



JGR Space Physics

RESEARCH ARTICLE

10.1029/2024JA032708

Key Points:

- We proposed a complete method for measuring ionospheric field-aligned currents (FACs)
- Within the auroral oval, both heightintegrated conductance gradients and vorticities play equally important roles
- In non-auroral regions, vorticities take on a dominant role in influencing FACs

Correspondence to:

J. Y. Lu, jylu@nuist.edu.cn

Citation:

Qu, B. H., Lu, J. Y., Wang, Z. W., Liu, J. J., Wang, M., Li, J. Y., & Zhang, H. (2024). Estimation of ionospheric field-aligned currents using SuperDARN radar and DMSP observations. *Journal of Geophysical Research: Space Physics*, 129, e2024JA032708. https://doi.org/10.1029/2024JA032708

Received 1 APR 2024 Accepted 21 MAY 2024

Estimation of Ionospheric Field-Aligned Currents Using SuperDARN Radar and DMSP Observations

B. H. Qu¹, J. Y. Lu¹, Z. W. Wang², J. J. Liu³, M. Wang¹, J. Y. Li¹, and H. Zhang¹

¹School of Atmospheric Physics, Institute of Space Weather, Nanjing University of Information Science and Technology, Nanjing, China, ²State Key Laboratory of Marine Geology, School of Ocean and Earth Science, Tongji University, Shanghai, China, ³MNR Key Laboratory for Polar Science, Polar Research Institute of China, Shanghai, China

Abstract Studies commonly assumed that variations in ionospheric conductance were insignificant and proposed that vorticities can be a reliable proxy or diagnostic for ionospheric field-aligned currents (FACs). We propose a complete method for measuring FACs using data from the Super Dual Auroral Radar Network radar and the Defense Meteorological Satellite Program. In our method, the FACs are determined by three terms. The first term is referred to as magnetospheric-origin FACs, while the second and third terms are known as ionospheric-origin FACs. This method incorporates height-integrated conductances based on observational data, thereby addressing the limitation of assuming uniform conductances. Different from previous works, we can calculate FACs at a low altitude of 250 km and obtain high-resolution measurements within observable areas. Another advantage of this method lies in its ability to directly calculate and analyze the impact of ionospheric vorticity and conductance on FACs. We apply this method to obtain FACs in the Northern Hemisphere from 2010 to 2016 and analyze the distributions of height-integrated conductances and total FACs. Our analysis reveals that the average FACs clearly exhibit the large-scale R1 and R2 FAC systems. We conduct statistical analysis on magnetospheric-origin FACs and ionospheric-origin FACs. Our findings show that within the auroral oval, ionospheric-origin FACs reach a comparable level to magnetospheric-origin FACs. However, ionospheric-origin FACs are significantly minor and almost negligible in other regions. This implies that heightintegrated conductance gradients and vorticities play equally significant roles within the auroral oval, whereas vorticities dominate in other regions.

Plain Language Summary Field-aligned currents (FACs) refer to current sheets that flow parallel or antiparallel to the geomagnetic field lines in the polar region. Typically, the intensity of FACs is estimated using magnetic perturbation measurements, while the current density is determined by the thickness of current sheets. In this study, we propose another method for calculating FACs based on ionospheric plasma vorticities and conductances. This method allows for FAC calculations at lower altitudes compared to previous methods. Additionally, we investigate the significance of vorticities and height-integrated conductance gradients on FACs. Our findings reveal that both height-integrated conductance gradients and vorticities significantly influence FACs in auroral emission areas. However, the influence of vorticities is more pronounced in other areas.

1. Introduction

There are various transport mechanisms for energy and momentum between the magnetosphere and ionosphere. One significant way is through field-aligned currents (FACs), also known as Birkeland currents. Extensive research has been conducted on the intensity and large-scale structure of FACs for several decades (Gjerloev et al., 2011; Iijima & Potemra, 1976a; Wang & Lühr, 2021; Wang et al., 2005; Zmuda & Armstrong, 1974). The distribution of FACs is primarily influenced by the direction of the interplanetary magnetic field (IMF). At the same time, the FAC intensity is affected by the electric field and ram pressure of the solar wind, as well as ionospheric conductance (Korth et al., 2010). When the IMF is southward, FACs exhibit a pattern of Region 1 (R1) and Region 2 (R2) currents (Iijima & Potemra, 1976a, 1976b). Under northern IMF conditions, an additional current system, commonly known as the "NBZ" or "Region 0" currents, is frequently detected in the dayside cusp region (Iijima et al., 1984; Milan et al., 2000, 2017).

Early studies on FACs utilized magnetometer measurements obtained from low Earth orbital or polar-orbit satellites such as Triad, OGO 5 (Orbiting Geophysical Observatory), Dynamics Explorer, Ørsted, and CHAMP (Challenging Minisatellite Payload). These studies combined the magnetic perturbation data, calculated

© 2024. American Geophysical Union. All Rights Reserved.

OU ET AL. 1 of 15



by observations of these satellites, with Ampère's law $(\nabla \times \vec{B} = \mu_0 \vec{J})$ to determine the FAC density (Wang et al., 2005). For instance, Wang et al. (2005) investigated the characteristics of FACs in the Southern Hemisphere using magnetic field data from the CHAMP satellite. Juusola et al. (2014) analyzed the distributions of FACs and convections under various IMFs by combining magnetic field data from the CHAMP satellite with convection data from the Super Dual Auroral Radar Network (SuperDARN) radars. Additionally, the magnetic field data from the DE 2 and Ørsted satellites are also used to model FACs (Papitashvili et al., 2002; Weimer, 2001). With advancements in satellite technology, such as Cluster II, ST5, and Swarm satellites, the FAC density can be estimated by simultaneous measurements of multiple satellites (Xiong et al., 2020). Research on FACs, based on multi-satellite observation technology, primarily focuses on the effects of solar wind and IMF, the dynamic evolution of FACs during magnetic storms and substorms, as well as the distribution characteristics of FACs (Dunlop et al., 2015; Escoubet et al., 2001; Gjerloev et al., 2011; Ritter et al., 2013; Slavin et al., 2008; Wang & Lühr, 2021; Wang et al., 2020). Moreover, the Active Magnetosphere and Planetary Electrodynamics Response Experiment (AMPERE) is another significant application of the multi-satellite method for calculating FACs (Anderson et al., 2000; Green et al., 2009; Korth et al., 2010). The FAC data provided by AMPERE is widely used in studies investigating substorm current wedges and the relationship between FACs and aurora (Carter et al., 2016; Coxon et al., 2014a, 2014b; Robinson et al., 2018).

Considering the limitations of spacecraft measurements under certain conditions, it is highly valuable to calculate FACs using alternative methods. In addition to utilizing magnetic perturbation data from spacecraft measurements, FACs can be accurately determined by ionospheric convection electric fields and conductances. However, measuring or modeling spatiotemporal variations in ionospheric conductances is challenging. Conductances depend not only on solar photoionization but also on auroral particle impact ionization (McGranaghan, Knipp, Matsuo, et al., 2015; McGranaghan, Knipp, Solomon, & Fang, 2015). Robinson and Vondrak (1984) established a connection between solar ionization and conductance by considering parameters such as the solar zenith angle, season, and level of solar flux ($F_{10.7}$). Then, Robinson et al. (1987) proposed a model for height-integrated conductances based on electron precipitation (referred to as the Rob87 model in our article). More recently, the GLobal AirglOW (GLOW) model has incorporated a section to calculate height-integrated conductances (McGranaghan, Knipp, Solomon, & Fang, 2015; Solomon, 2017).

To facilitate the study of FACs, previous studies commonly assumed that variations in ionospheric conductance were insignificant and could be ignored (Chisham et al., 2009; Freeman et al., 1990; McWilliams et al., 2001; Sofko et al., 1995). These studies also proposed that vorticities can be a reliable proxy or diagnostic for FACs. Freeman et al. (1990) first combined this assumption with observations from the SABRE radar to estimate FACs. Subsequently, Sofko et al. (1995) utilized the Super Dual Auroral Radar Network velocity measurements to determine convection vorticities and used them as a proxy for FACs. They found that upward FACs in the postnoon sector corresponded to the bright aurora, while downward FACs were located on both sides of the bright auroral region. McWilliams et al. (2001) also employed this approximation and expanded the vorticity map to cover the entire polar region. They discovered that the distribution of FACs was consistent with the dayside current wedge in the footprint of the dayside magnetic reconnection region.

This paper proposes a complete method for calculating FACs based on vorticities and conductances. Our approach involves determining vorticities through SuperDARN line-of-sight velocities and deriving conductances from the GLOW model. Moreover, there is a debate about whether vorticities are a good proxy for FACs because the change in conductance is typically not negligible (Amm et al., 2005; Green et al., 2006; Kosch et al., 2001). To address this issue, we discuss the significance of vorticities and height-integrated conductance gradients in FACs. This paper is laid out as follows. Section 2 provides a detailed explanation of the methods and data employed to calculate ionospheric vorticities, conductances, and FACs. In Section 3, we discuss the distribution of average FACs and compare variations in each FAC component. These findings are further discussed in Section 4, and the paper concludes in Section 5.

2. Data and Methods

2.1. Introduction to Methodology

Here, we describe a method for calculating FACs based on ionospheric plasma velocities and conductances. FACs are closely associated with the horizontal Pedersen and Hall currents in the ionosphere. Assuming that the

QU ET AL. 2 of 15

total ionospheric current system has no divergence ($\nabla \cdot \boldsymbol{J} = 0$, where \boldsymbol{J} represents the total ionospheric current), FACs can be estimated by the divergence of horizontal currents (Boström, 1974). Hence, the FAC density (J_{\parallel}) can be expressed as

$$J_{\parallel} = \sum_{P} \nabla \cdot \boldsymbol{E} + \boldsymbol{E} \cdot \nabla \sum_{P} + \hat{\boldsymbol{B}} \times \boldsymbol{E} \cdot \nabla \sum_{H}$$
 (1)

where E is the ionospheric electric field, \sum_P and \sum_H are the height-integrated Pedersen and Hall conductances, respectively, and \hat{B} is the unit vector of the geomagnetic field. In Equation 1, J_{\parallel} is considered positive when the current flows in the direction of the magnetic field, which means downward into the ionosphere in the Northern Hemisphere. Previous studies commonly consider Equation 1 as a combination of two types of FACs: (a) Magnetospheric-origin FACs (first term in Equation 1), which are caused by changes in the imposed electric field, and (b) Ionospheric-origin FACs (second and third terms in Equation 1), which are generated by the spatial distribution of ionospheric conductances (Chisham et al., 2009).

According to the connection between drift velocity and electric field $(V = (E \times B)/B^2)$, Equation 1 can be rewritten as

$$J_{\parallel} = -\sum_{P} \mathbf{B} \cdot \nabla \times \mathbf{V} + (\mathbf{V} \times \mathbf{B}) \cdot \nabla \sum_{P} + |\mathbf{B}| \mathbf{V} \cdot \nabla \sum_{H}$$
 (2)

where V is the drift velocity, B is the geomagnetic field, and $\omega = \nabla \times V$ is the ionospheric vorticity. Therefore, FACs can be calculated based on conductances, velocities, vorticities, and geomagnetic fields.

2.2. Data Set

This study utilizes SuperDARN and Defense Meteorological Satellite Program (DMSP)/Special Sensor Ultraviolet Spectrographic Imager (SSUSI) data sets. These data sets offer a range of parameters that can be employed to calculate FACs. In this section, we describe the sources and processing methods of these data sets.

We utilize line-of-sight velocity measurements from the SuperDARN high-frequency radars to estimate ionospheric vorticities. SuperDARN is a network of coherent scatter radars that observe the polar ionosphere and parts of the high-latitude ionosphere in both the Northern and Southern Hemisphere. These radars transmit and receive radio signals within a frequency range of 8–20 MHz, allowing us to measure the line-of-sight velocity of density irregularities that move at the drift velocity in the F-region (Villain et al., 1985). In this study, we utilize observations from high-latitude radars located in the Northern Hemisphere (Prince George, Kodiak, Kapuskasing, Saskatoon, Goose Bay, Stokkseyri, Hankasalmi, and Pykkvibaer). Our database collects observations limited to the common modes of these radars during the years 2010–2016. The velocity error threshold is set at 200 m/s to ensure data quality. Additionally, we remove observations with $|V_{los}| \leq 35$ m/s and $|width| \leq 30$ m/s to exclude the influence of ground backscatter (Chisham & Pinnock, 2002; Liu et al., 2012).

Conductance is another crucial parameter for calculating FACs. Electron precipitation measurements from the DMSP/SSUSI (Paxton & Anderson, 1992; Paxton & Zhang, 2016) are necessary for determining ionospheric conductances. The SSUSI instrument consists of a line scanning imaging spectrograph with a spectral range of 115–180 nm and a nadir photometer system. It observes approximately 1/3–1/2 of the polar ionospheres and captures data in five spectral bands: HI-Lyman α (121.6 nm), OI (130.4 nm), OI (135.6 nm), N2-LBHS (140–150 nm), and N2-LBHL (165–180 nm) (Paxton et al., 2002). Assuming that the precipitating particles consist solely of electrons, the observations from the Lyman-Birge-Hopfield (LBH) long (165–180 nm) and short band (140–150 nm) can be used to calculate the characteristic energy and energy flux of particle precipitation (Carter et al., 2020). A comprehensive description of the data processing algorithms can be found in the SSUSI data products algorithm document v1_13. It is worth noting that this algorithm assumes that the energy of particle precipitation follows a Gaussian distribution. While this assumption may introduce minor errors in determining characteristic energy and energy flux, Carter et al. (2020) have discussed this. In this study, we collect the characteristic energy and energy flux data of particle precipitation from all available SSUSI files between 2010 and 2016 for the DMSP F16, F17, and F18 spacecraft. These data are used as input parameters for the GLOW model to obtain ionospheric conductances (see Section 2.4 for details). Additionally, to remove the impact of

QU ET AL. 3 of 15

21699402, 2024, 6, Downloaded from https://agupubs.onlinelibrary.wiley.com/doi/10.1029/2024JA032708 by Southwest Research Institute,

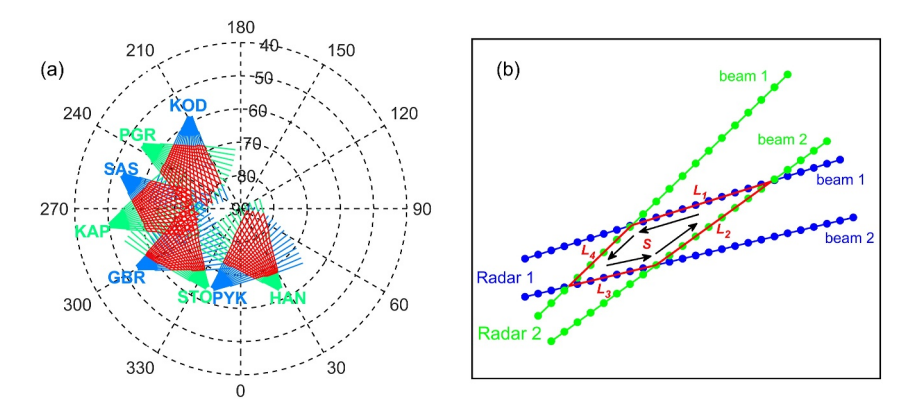


Figure 1. (a) The fields of view of eight Northern Hemisphere Super Dual Auroral Radar Network radar radars in Altitude-Adjusted Corrected Geomagnetic coordinates. The beam directions of radars are represented by green and blue lines, while the red grids indicate the overlapping fields of view from adjacent radars. (b) The schematic diagram of the quadrilateral measurement cell. The beams of Radar 1 and Radar 2 are depicted by blue and green lines, respectively. The four beams overlap to form a quadrilateral measurement cell, shown in red. The green and blue points along these beams represent the locations of velocity measurements. The closed path C is formed by four line segments (L_1 , L_2 , L_3 , and L_4), and the surface surrounded by this closed path is denoted as S.

background noise and airglow, only the data with radiances greater than 100 R and energy flux greater than $0.2 \text{ erg cm}^{-2} \text{ s}^{-1}$ in both LBH bands are kept.

In addition to the SuperDARN and DMSP/SSUSI observational data, we also use the geomagnetic field data and the 10.7 cm solar radio flux data ($F_{10.7}$ index) from 2010 to 2016. The $F_{10.7}$ data is sourced from the geomagnetic and solar databases at the NOAA Space Weather Prediction Center. The values of geomagnetic fields are determined by the International Geomagnetic Reference Field (IGRF) model (Thébault et al., 2015).

2.3. Vorticity Measurement Method

This section describes how to use line-of-sight velocity measurements to calculate ionospheric plasma vorticities. These measurements are derived from four Northern Hemisphere SuperDARN radar pairs between 2010 and 2016. Figure 1a illustrates the fields of view of these eight radars in the Altitude-Adjusted Corrected Geomagnetic (AACGM) coordinates. These fields of view are determined using the empirical virtual height model developed by Chisham et al. (2008). As shown in Figure 1a, each SuperDARN radar consists of 16 beams represented by blue or green solid lines. The length of these solid lines corresponds to the number of SuperDARN range gates, which are typically 75 or 225 gates. Moreover, the red grid indicates the overlapping fields of view from adjacent radars and covers almost half of the polar regions. Therefore, the line-of-sight velocity measurements are abundant enough to calculate vorticities in the majority of polar regions.

The method employed in this study to quantify vorticities is similar to that described by Chisham et al. (2009). To calculate vorticities, we apply Stokes' theorem:

$$\oint_{\mathcal{C}} V \cdot dl = \int_{\mathcal{S}} \omega \cdot dS \tag{3}$$

where C is a closed path, and S is the surface surrounded by the closed path C. In this method, we utilize quadrilateral measurement cells defined by the beams of SuperDARN radars. In Figure 1a, the red grid represents these measurement cells. Figure 1b shows the schematic diagram of a quadrilateral measurement cell, where the blue and green solid lines represent the beams of radar 1 and radar 2, respectively. The red lines highlight the surrounding region of the four beams, forming the quadrilateral measurement cell. Within this cell, a closed path C is formed by the four line segments (L_1 , L_2 , L_3 , and L_4). The green and blue points on these beams indicate the locations of velocity measurements. Furthermore, the black arrows represent the directions of velocities when the vorticity is positive.

OU ET AL. 4 of 15

'agupubs.onlinelibrary.wiley.com/doi/10.1029/2024JA032708 by Southw

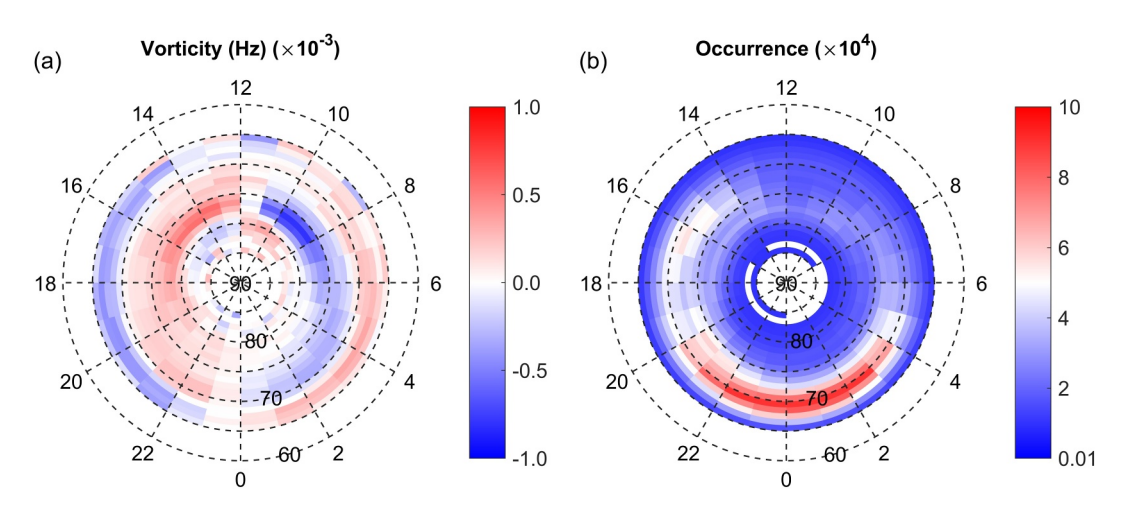


Figure 2. (a) The spatial distribution of average vorticities measured by the eight Northern Hemisphere Super Dual Auroral Radar Network radar radars from 2011 to 2013. (b) The number of measurements used to calculate the average vorticity in each bin. The distribution is presented in 1° Altitude-Adjusted Corrected Geomagnetic latitude bins by 1 hr of magnetic local time

Due to the line-of-sight velocity parallel or anti-parallel to the beam, $\oint_c V \cdot dl$ can be rewritten as $\oint_c \pm v dl$ (the "±" sign indicates opposite or the same direction). In the polar regions, the geomagnetic field aligns closely with the vertical direction, so we assume that the magnetic field is vertically downward. Therefore, in quadrilateral measurement cells, Stokes' theorem can be rewritten as follows:

$$\omega_{\parallel} = -\frac{\sum_{i=1}^{4} v_{i\perp} l_i}{S} \tag{4}$$

here ω_{\parallel} represents the vorticity aligned with the geomagnetic field, S is the area of the surface enclosed by the closed path C, $l_i(i=1,2,3,4)$ is the length of the line segment that forms the closed path C, and $v_{i\perp}$ is the mean velocity perpendicular to the geomagnetic field. In Equation 4, the "—" sign indicates that the vorticity is considered positive when it is direct along the geomagnetic field in the Northern Hemisphere. The location of vorticity is defined as the geometric center of the quadrilateral measurement cell. Furthermore, the vorticity is located at an altitude of 250 km, which corresponds to the approximately constant altitude of the SuperDARN line-of-sight velocity measurements in the F region ionosphere.

The vorticity values from 2011 to 2013 are organized into spatial bins based on magnetic local time (MLT) and AACGM latitude. Each bin represents a 1-hr MLT by 1-degree magnetic latitude (MLAT) range. In order to create an average vorticity map, we calculate the average vorticity within each spatial bin. Figure 2 presents the average vorticities and the number of measurements in the Northern Hemisphere. It is worth noting that only spatial bins with more than 100 measurements are shown in Figure 2. Figure 2b reveals that most bins have more than 10^4 measurements, ensuring the reliability of average vorticities. In Figure 2a, the red shading represents positive (downward) vorticities, while the blue shading represents negative (upward) vorticities. The average vorticity map shows characteristics similar to the distribution map of average FACs. Additionally, a vorticity structure resembling NBZ FACs can be observed near 80° MLAT on the sunside. Therefore, the overall distribution of average vorticities resembles the NBZ/R1/R2 system observed in average FACs. This similarity is one of the main reasons why vorticities are frequently used as a proxy for FACs in the ionosphere (Chisham et al., 2009). Moreover, our statistical results are consistent with the result of Chisham et al. (2009).

2.4. Conductance Measurement Method

This section outlines the method for calculating height-integrated conductances using the GLOW model. The GLOW model is a tool commonly used to analyze the physical processes of dayglow, nightglow, and aurora (Bailey et al., 2002; Solomon, 2017; Solomon & Abreu, 1989; Solomon et al., 1988). It operates on background

QU ET AL. 5 of 15

neutral and ionized atmospheres, which are influenced by the incoming energy from the Sun and aurora. The background atmospheres are based on the standard Naval Research Laboratory Mass Spectrometer Incoherent Scatter Radar (NRLMSISE-00) model (Picone et al., 2002) and the International Reference Ionosphere model (Bilitza & Rawer, 1992). The GLOW model also incorporates a background ionization source, referred to as the background "nighttime" ionization. This ionization is derived from the Thermosphere-Ionosphere General Circulation Model (Roble et al., 1988) and takes into account the influence of the stellar background and multiple scattering of solar atomic hydrogen emissions in the geocorona (Strobel et al., 1980). Consequently, there are always some non-zero conductances present in the polar ionospheres. However, their contribution remains relatively insignificant compared to the conductances resulting from auroral electron precipitation. Therefore, the impact of background ionization is considered insignificant. For more detailed information on the GLOW model, please refer to Solomon (2017).

The GLOW model incorporates various inputs such as date, UT, latitude, longitude, $F_{10.7}$, $< F_{10.7} >$, characteristic energy, and total energy flux of auroral electron precipitation. In this article, the auroral electron precipitation is obtained from the LBH long (165-180 nm) and short band (140-150 nm) radiances observed by SSUSI. Moreover, to remove background noise and airglow in the SSUSI data, only observations with radiances greater than 100 R and energy flux greater than 0.2 erg cm⁻² s⁻¹ in both LBH bands are considered. It is important to note that the energy distribution of auroral electron precipitation in the GLOW model follows a Maxwellian distribution. However, the SSUSI data has been calculated based on the assumption that the energy of electron precipitation follows a Gaussian distribution. To align with this, the file (maxt.f90) that generates Maxwellian spectra in the GLOW model is modified to generate Gaussian spectra. The Gaussian distribution formula used in this paper is as follows:

$$\Phi_{e0} = \left[\frac{Q_0}{\pi^{3/2}WE_0}\right] \exp\left[-\left(\frac{E - E_0}{W}\right)^2\right] \tag{5}$$

here, Φ_{e0} is the electron flux, E_0 is the characteristic energy, Q_0 is the energy flux, and W is the width parameter (usually 0.15E₀). The GLOW model outputs are presented in Table 1 of Solomon (2017). In our study, we utilize the Pedersen and Hall conductances calculated by the GLOW model to determine \sum_{P} and \sum_{H} between 80 and 250 km.

In order to ensure the reliability of conductances obtained from the GLOW model, we analyze an example of height-integrated conductances based on SSUSI auroral emission data. Figure 3 presents observations from the DMSP/SSUSI F17 (a-c) and the corresponding height-integrated conductances (d-e) in the Northern Hemisphere polar regions during the period 12.6 UT-13.0 UT on 3 January 2010. Intense auroral activity occurs on both the downside and dusk side, as shown in Figure 3c. The energy flux (Figure 3a) and characteristic energy of auroral electron precipitation (Figure 3b) exhibit similar distribution characteristics. Moreover, Figure 3f displays \sum_{P} derived from solar radiation, and we observe that the distribution of \sum_{P} is consistent with that of solar illumination. To further analyze the credibility of height-integrated conductances derived from the GLOW model, we compare them with the results obtained from the Rob87 model (Carter et al., 2020, 2023; Robinson et al., 1987). The \sum_{P} calculated by the GLOW model and the Rob87 model are shown in Figures 3d and 3e, respectively. Both of them exhibit similar distribution characteristics. However, the Rob87 model overestimates \sum_{P} compared to the GLOW model, with an average difference of approximately 1.7 S. This difference may be attributed to the Gaussian assumption of auroral electron precipitation or the limitations of the models. However, this difference is not significant compared to the values of height-integrated conductances. In conclusion, these comparisons and results further support the reliability of height-integrated conductances derived from the GLOW model.

3. Results

In order to verify our method, a case verification is conducted as depicted in Figure 4. The results from our method and AMPERE are shown in Figures 4a and 4b, with red and blue shading indicating downward and upward FACs, respectively. It can be seen that there is consistency in their distributions. We also obtain the FACs of AMPERE at the same MLTs and MLATs as our method's result using an interpolation method. Figure 4c shows a direct comparison between them. The comparison indicates that most data points are near the dashed line, although some differences exist. These discrepancies may be attributed to differences in height (ours at 250 km and

OU ET AL. 6 of 15

21699402, 2024, 6, Downloaded from https://agupubs.onlinelibrary.wiley.com/doi/10.1029/2024/A032708 by Southwest Research Institute, Wiley Online Library on [02/04/2025]. See the Terms

are governed by the applicable Creati

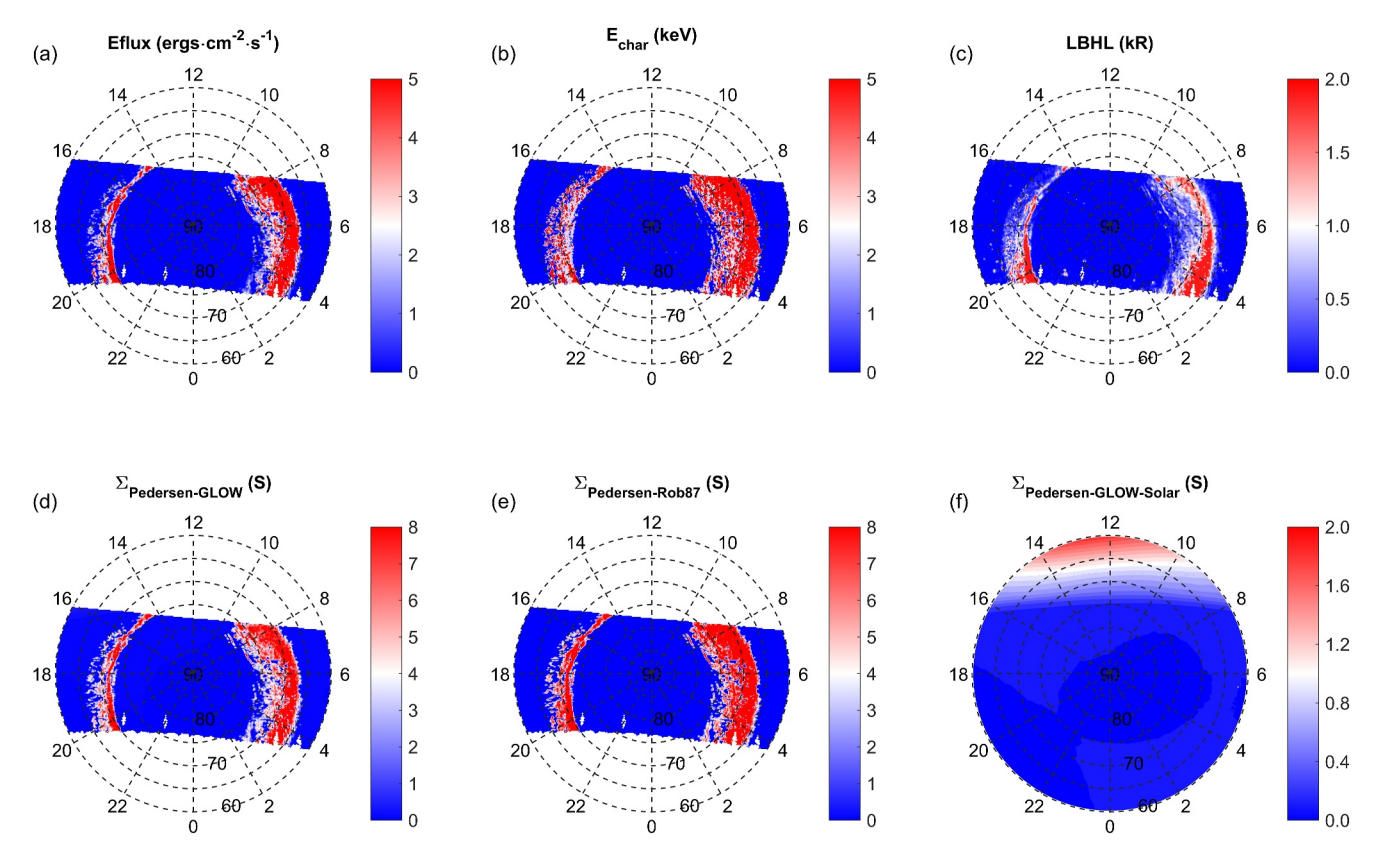


Figure 3. The height-integrated conductances and observations obtained by DMSP/SSUSI F17 in the Northern Hemisphere polar regions during the period 12.6 UT–13.0 UT on 3 January 2010. The observations from the SSUSI instrument include the energy flux (a), the characteristic energy (b), and the auroral emissions of the LBHL band (c). \sum_{P} derived from auroral electron precipitation (d) and solar radiation (f) are calculated by the GLOW model. Additionally, \sum_{P} is determined based on SSUSI auroral emission data and the Rob87 model (e).

AMPERE at 780 km) and the impact of conductance. Therefore, this comparison and the consistency in the distributions can validate the reliability of our approach.

Figure 5 illustrates the coverage of DMSP F16-F18 satellite orbits, the total number of FAC measurements, and the distribution of FAC measurements' number under various geomagnetic levels in the Northern Hemisphere from 2010 to 2016. As depicted in Figure 5a The DMSP satellite orbits predominantly cover the dawnside and duskside. Despite the broad band of observations provided by each scan of the DMSP satellite, as shown in Figure 3, nighttime observations in the Northern Hemisphere remain incomplete. We calculate FAC data from

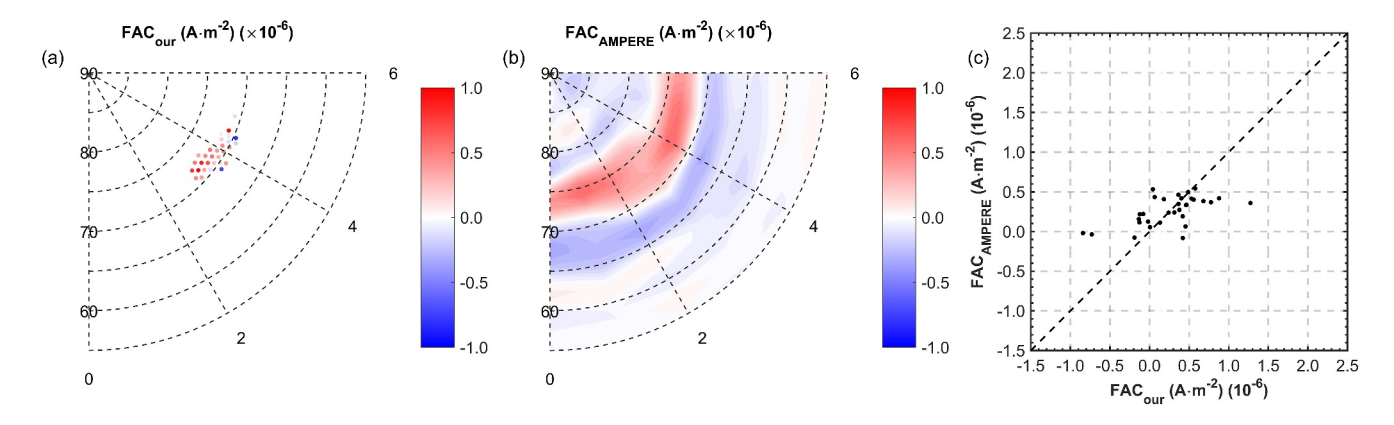


Figure 4. The distributions (a, b) and comparison (c) of field-aligned currents from our approach and Active Magnetosphere and Planetary Electrodynamics Response Experiment in the Northern Hemisphere polar regions during the period 13.8 UT–14.0 UT on 27 April 2012.

QU ET AL. 7 of 15

21699402, 2024, 6, Downloaded from https://agupubs.onlinelibrary.wiley.com/doi/10.1029/2024/A032708 by Southwest Research Institute, Wiley Online Library on [02/04/2025]. See the Terms

are governed by the applicable Creativ

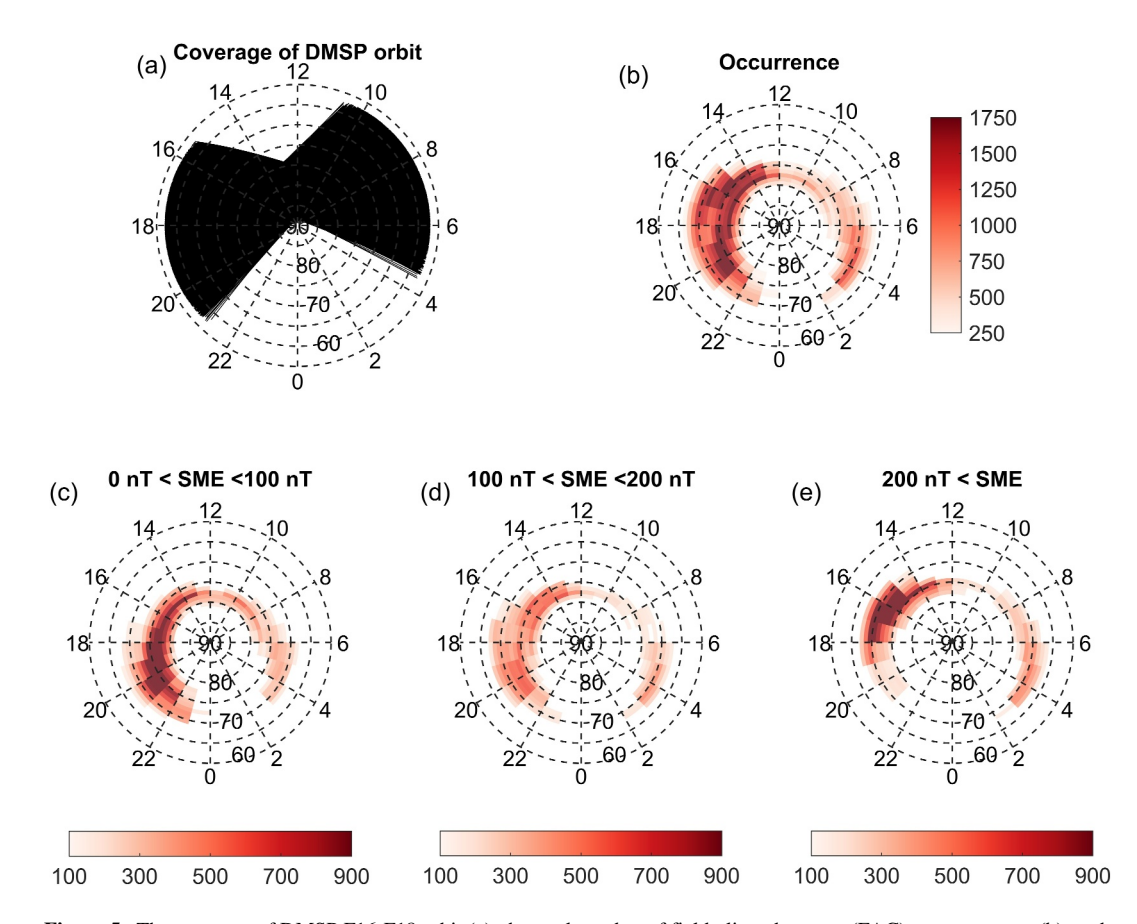


Figure 5. The coverage of DMSP F16-F18 orbit (a), the total number of field-aligned current (FAC) measurements (b), and the FAC measurements' number of different geomagnetic activity levels (c, d, e) in the Northern Hemisphere between 2010 and 2016.

2010 to 2016 using data from DMSP F16, F17, and F18 satellites. The number of FAC measurements, as presented in Figure 5b, are concentrated on both the dawnside and duskside. Figures 5c–5e display the number of FAC measurements under different levels of geomagnetic activity. It is evident that during periods of low magnetic disturbance, the results primarily focus on the high-latitude region of 18–22 MLT. However, during strong magnetic disturbances, the results are predominantly located in the high-latitude area of 14–18 MLT.

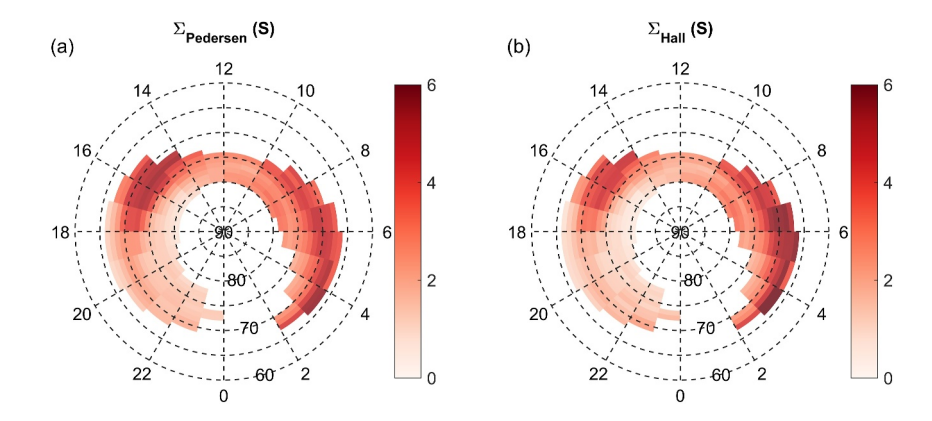


Figure 6. The distributions of average \sum_{P} (a) and average \sum_{H} (b) in the Northern Hemisphere between 2010 and 2016. The format and coordinate system of the plots are the same as in Figure 2.

QU ET AL. 8 of 15

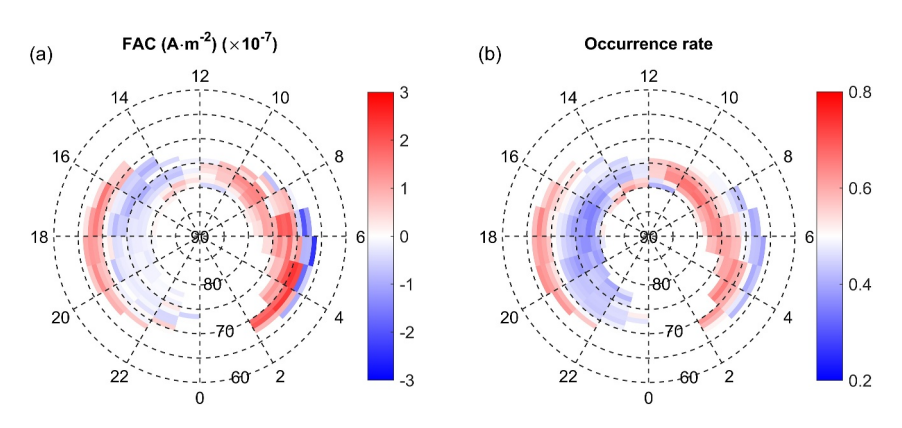


Figure 7. The average field-aligned currents (FACs) (a) and the occurrence rate of downward FACs (b) in the Northern Hemisphere between 2010 and 2016. The format and coordinate system of the plots are the same as in Figure 2.

A statistical analysis of height-integrated conductances and average FACs is also presented in Figures 6 and 7. Figure 6 illustrates the spatial distributions of averaged Σ_P and Σ_H in the Northern Hemisphere from 2010 to 2016. The results from Figure 6 demonstrate consistent characteristics for both Σ_P and Σ_H . Specifically, in the afternoon sector, the peak of average height-integrated conductances is observed near 73° MLAT. However, in the predawn sector, the average height-integrated conductances increase as MLAT decreases. This phenomenon may be attributed to the lack of measurement data at low MLATs. Additionally, there are differences in the values of Σ_P and Σ_H , particularly in the predawn sector where Σ_H is significantly higher than Σ_P . In comparison with the findings of McGranaghan, Knipp, Matsuo, et al. (2015) and McGranaghan, Knipp, Solomon, & Fang (2015), our statistical results show a notable increase in the afternoon. This can be attributed to the abundance of strong geomagnetic activity data in our statistical results during the afternoon, as depicted in Figure 5. In addition, there are smaller mean Hall conductances prior to midnight in our results due to the inclusion of a significant amount of low geomagnetic activity in our statistics. In principle, our findings on the dawnside align with those of McGranaghan, Knipp, Matsuo, et al. (2015) and McGranaghan, Knipp, Solomon, & Fang (2015).

In Figure 7, a series of images is presented to show the average FACs, the occurrence rate of downward FACs, and the number of FAC measurements in the Northern Hemisphere from 2010 to 2016. Figure 7a displays the spatial distribution of average FACs in the Northern Hemisphere. The red shading indicates downward FACs, while the blue shading indicates upward FACs. The map of average FACs reveals a clear large-scale structure: (a) Between 70° and 80° MLAT, downward (upward) FACs occur in the dawn (dusk) sector, corresponding to the R1 FACs; (b) Below 70° MLAT, the dusk (dawn) sector is characterized by downward (upward) FACs, corresponding to the R2 FACs. Figure 7b presents the rate of downward FACs in the Northern Hemisphere. This occurrence rate is calculated as the ratio between the number of downward FAC measurements and the total number of FAC measurements. The red (blue) shading indicates that the occurrence rate of downward (upward) FACs exceeds 50%. As shown in Figure 7b, between 70° and 80° MLAT in the dawn (dusk) sector, the downward (upward) FACs are more likely to occur. Similarly, below 70° MLAT in the dawn (dusk) sector, there is a higher likelihood of upward (downward) FACs. These characteristics also correspond to the R1/R2 FACs. What needs illustration is that the statistical results only include spatial bins with more than 250 measurements.

Figures 8a and 8b illustrate the variations of height-integrated conductances with AACGM latitude in the dawn and dusk sectors. These figures clearly show that both \sum_P and \sum_H follow a pattern of initially increasing and then decreasing as MLAT increases. The peak in the dawn sector occurs at 67° – 68° MLAT, whereas the peak in the dusk sector occurs at 71° – 72° MLAT. Furthermore, \sum_H is significantly larger than \sum_P in the dawn sector, while there is minimal difference between them in the dusk sector. Figures 8c and 8d display the changes of FACs with AACGM latitude in the dawn and dusk sectors. In the dawn sector, R1 FACs (positive values) are observed in areas with MLAT greater than 68° , while R2 FACs (negative values) are observed in areas with MLAT less than 68° . This indicates that the transition area of R1/R2 FACs is approximately 68° . It seems lower than the average latitude of previous studies. However, the distribution of the FACs in Figure 7a is similar to Juusola et al. (2014). This discrepancy may be due to the majority of the data being collected in the 2–7 MLT, as shown in Figures 5b and 7a. The presence of SuperDARN backscatter during periods of strong geomagnetic activity may also be a

QU ET AL. 9 of 15

21699402, 2024, 6, Downlo

agupubs.onlinelibrary.wiley.com/doi/10.1029/2024JA032708 by Southwest Re

Wiley Online Library on [02/04/2025]. See the Terms and Conditions

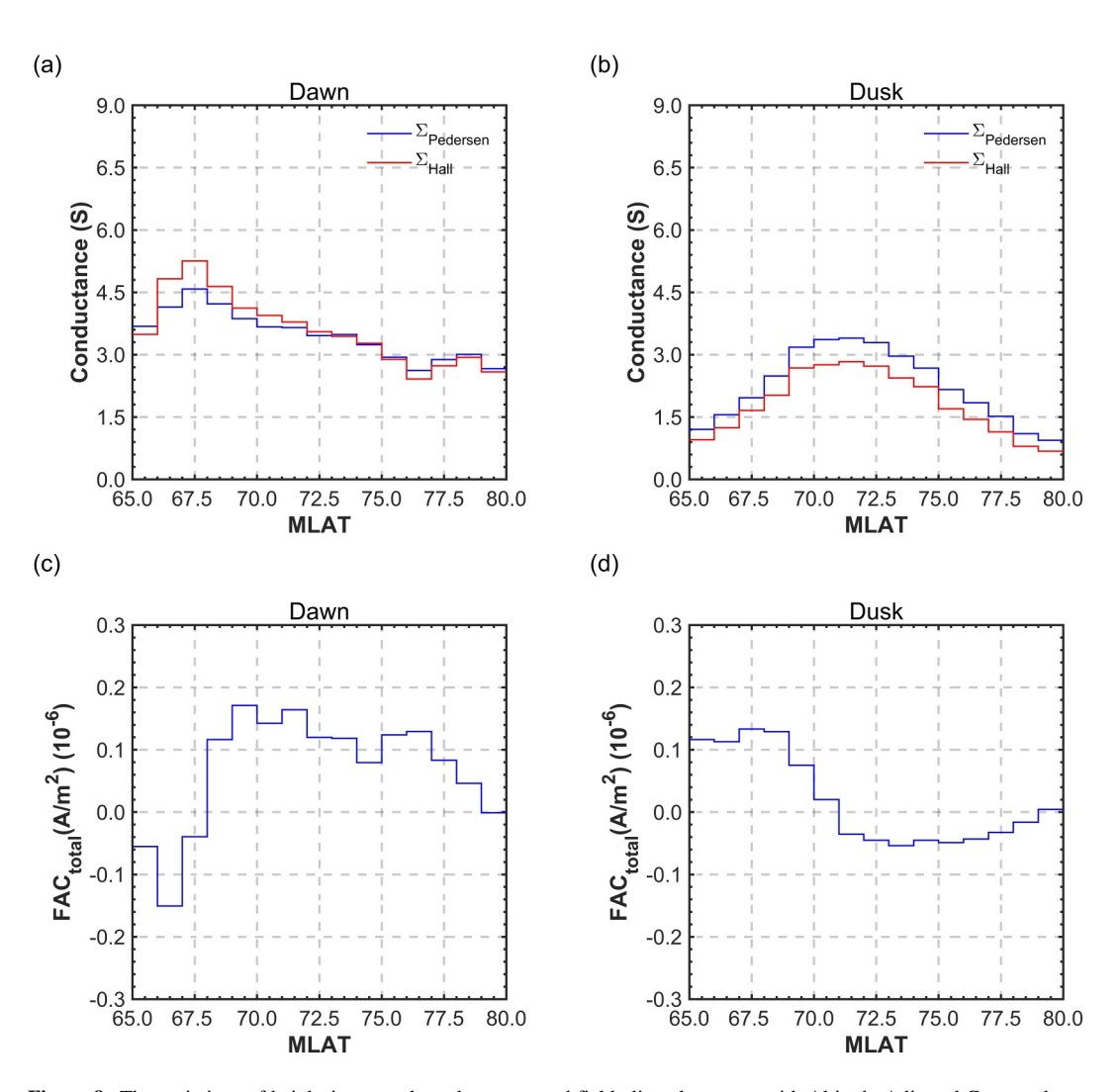


Figure 8. The variations of height-integrated conductances and field-aligned currents with Altitude-Adjusted Corrected Geomagnetic latitude in the dawn (a, c) and dusk (b, d) sectors.

significant factor. On the other hand, in the dusk sector, R1 FACs (negative values) are present in areas with MLAT greater than 71°, while R2 FACs (negative values) are present in areas with MLAT less than 71°. This suggests that the transition area of R1/R2 FACs is approximately 71°. The difference in the transition area between the dawn sector and the dusk sector may be attributed to the fact that the data in the dawn sector is primarily located in the predawn sector, whereas the data in the dusk sector is mainly collected in the afternoon sector.

Figures 9a and 9b depict the change in the characteristic energy and energy flux of auroral electron precipitation in relation to MLAT. It is observed that auroral electron precipitation occurs below 70° MLAT on the dawnside, while it occurs around 70° MLAT on the duskside. These phenomena indirectly suggest that there are enhanced auroral activities below 70° MLAT on the morning side and around 70° MLAT on the duskside. In our study, Equation 2 demonstrates that ionospheric-origin FACs are affected by height-integrated conductance gradients, whereas magnetospheric-origin FACs are primarily affected by vorticities. To further examine the importance of height-integrated conductance gradients in FACs, we analyze the variations of magnetospheric-origin FACs and ionospheric-origin FACs with AACGM latitude. Figure 9 shows that magnetospheric-origin FACs generally exhibit a structure similar to R1/R2 FACs. On the other hand, in the dawn and dusk sectors, ionospheric-origin FACs display high values at MLATs of 65°–69° and 67°–70°, respectively. At the same time, ionospheric-origin FACs reach a comparable level to magnetospheric-origin FACs in the high-value region, while they are significantly smaller and almost negligible in other regions. When comparing with the changes in characteristic energy and energy flux, it becomes evident that regions with high ionospheric FAC values correspond to intense

QU ET AL. 10 of 15

21699402, 2024, 6, Down

gupubs.onlinelibrary.wiley.com/doi/10.1029/2024JA032708 by Southwest

Institute, Wiley Online Library on [02/04/2025]. See the Terms

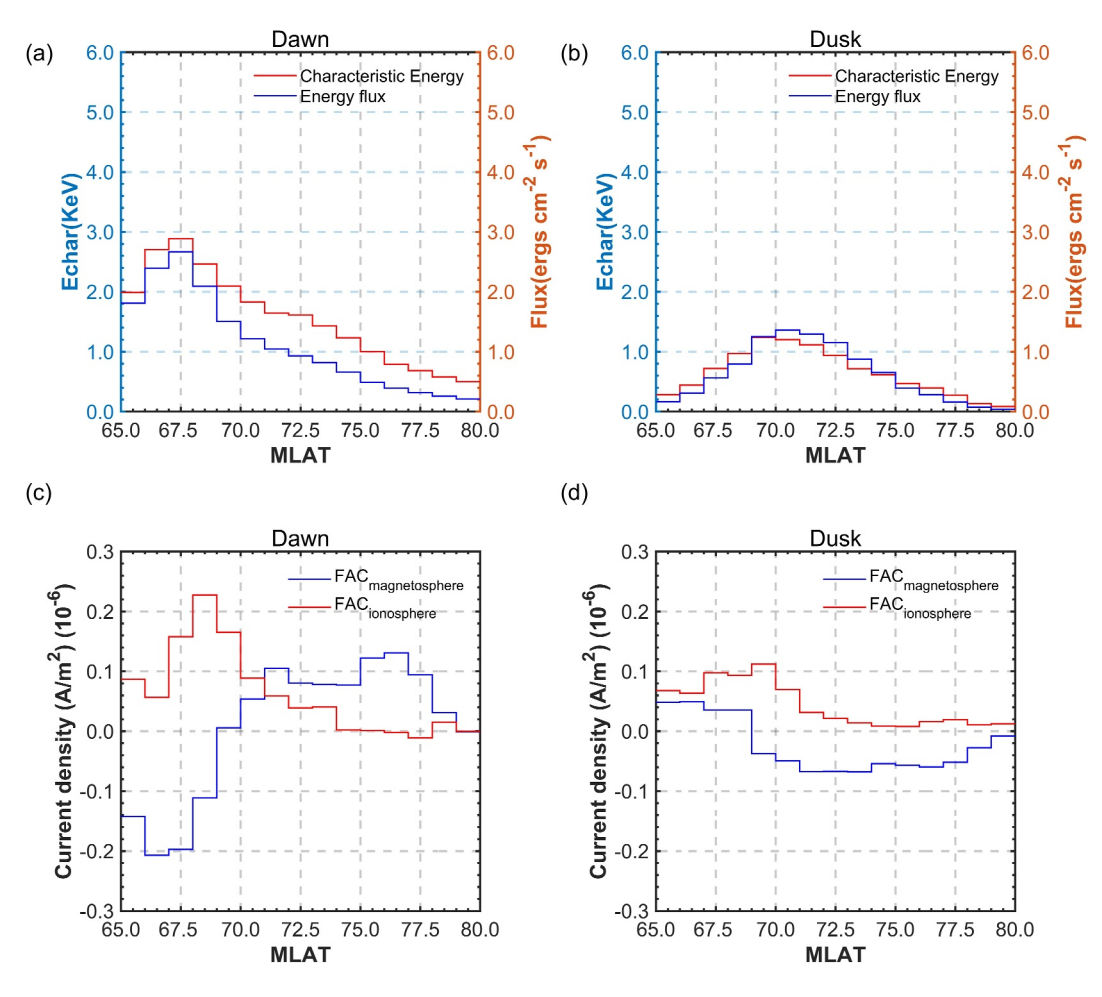


Figure 9. The variations of magnetospheric-origin field-aligned currents (FACs), ionospheric-origin FACs, the characteristic energy and energy flux with Altitude-Adjusted Corrected Geomagnetic latitude in the dawn (a, c) and dusk (b, d) sectors.

auroral electron precipitation. This observation further emphasizes the significant role of ionospheric FACs within intense aurora areas.

4. Discussion

This section provides a comprehensive discussion of FACs' calculation method and results. It also explores the advantages and limitations of this method in further detail. Additionally, we analyze the significance of height-integrated conductance gradients in FACs.

Assuming the total ionospheric current system is divergence-free, the FACs can be derived from the divergence of horizontal currents (Boström, 1974). This relationship is represented by Equation 1. By using the relationship between drift velocities and electric fields, the calculation formula for the FACs can be further rewritten as Equation 2. Therefore, the FACs can be determined using conductances, velocities, vorticities, and geomagnetic fields. In this study, geomagnetic fields are obtained through the IGRF model, while ionospheric plasma velocities are obtained through SuperDARN radar observations. Given the unavailability of direct observations for vorticities and conductances, we employ plasma velocity measurements and auroral electron precipitation to calculate these parameters. Figure 1 illustrates the observation grid composed of measurement cells. Vorticities can be calculated in these measurement cells by utilizing plasma velocities. As shown in Figure 2, the distribution of average vorticities exhibits a structure that closely resembles the NBZ/R1/R2 FAC systems and is highly consistent with the results of Chisham et al. (2009).

QU ET AL. 11 of 15

Early research on FACs was limited due to the lack of direct observations of conductances. However, recent studies have analyzed conductances using observations from the DMSP satellite (Carter et al., 2020, 2023; McGranaghan, Knipp, Matsuo, et al., 2015; McGranaghan, Knipp, Solomon, & Fang, 2015). In particular, Carter et al. (2020) calculated height-integrated conductances using empirical expressions from Robinson et al. (1987). Our study employs the GLOW model and the auroral electron precipitation data of DMSP/SSUSI to determine height-integrated conductances. It is worth noting that the precipitating particles are assumed to consist solely of electrons and to follow a Gaussian distribution in the DMSP/SSUSI data. This assumption may introduce errors in determining the characteristic energy, energy flux, and height-integrated conductances, as discussed by Carter et al. (2020, 2023). To evaluate the reliability of height-integrated conductances, a comparison is made between the results obtained from the Rob87 model and those derived from the GLOW model, as illustrated in Figure 3. The results of both models exhibit a consistent distribution of height-integrated conductances, with only minor numerical variations. Moreover, the distributions of average \sum_P (a) and average \sum_H also indicate that height-integrated conductances from the GLOW model are credible.

These conductances, in combination with vorticity data obtained from SuperDARN radars, are employed to determine FACs. Unlike previous methods that rely on magnetic field data from satellites (e.g., Dunlop et al., 2015; Escoubet et al., 2001; Gjerloev et al., 2011; Ritter et al., 2013; Slavin et al., 2008; Wang & Lühr, 2021; Wang et al., 2020), our method can calculate FACs at a lower altitude (250 km) and achieve higher resolution within a limited range. Another advantage of our method, in comparison to other approaches, lies in its ability to directly calculate and analyze the impact of ionospheric vorticity and conductance on FACs. However, our method may provide a smaller data set than the AMPERE data as it depends on joint observations from SuperDARN radars and DMSP satellites. In addition, we conduct a statistical analysis of height-integrated conductances and FACs obtained through our method. The results indicate that the distributions of \sum_{P} and \sum_{H} exhibit consistent characteristics. The distribution of average FACs reveals a clear large-scale structure: R1/ R2 FACs. However, it is observed in Figure 7 that the coverage of local time and MLAT is limited. This limitation can be attributed to two main reasons: (a) the inherent limitations of observation coverage of DMSP F16, F17, and F18 satellites, as shown in Figure 5; (b) our statistics only include observations from high-latitude radars. By incorporating observations from mid-latitude and polar radars, the coverage of magnetic latitudes may be expanded. Improving observations in the midnight sector may be achievable in the Southern Hemisphere. It is important to note that there is some noise in the statistical results. As illustrated in Figure 5, the geomagnetic activity levels vary across different regions. Thus, the noise may be due to combining data from various geomagnetic activity levels into a single FAC pattern. The influence of the conductance gradient may be another significant reason. Although magnetospheric-origin FACs exhibit no noise in the statistical results, the FACs introduce noticeable noise after incorporating the ionospheric-origin FACs. At the same time, the conductance gradient plays a crucial role in affecting ionospheric-origin FACs. Therefore, the conductance gradient might also significantly contribute to the noise.

Previous studies relied on using vorticities as a proxy for FACs due to the lack of direct observations of conductances (Chisham et al., 2009; Freeman et al., 1990; McWilliams et al., 2001; Sofko et al., 1995). However, the validity of using vorticities as a proxy for FACs is debatable as the required approximation of uniform conductances is often a poor assumption (Amm et al., 2005; Green et al., 2006; Kosch et al., 2001). In our method, Equation 2 demonstrates that ionospheric-origin FACs are affected by height-integrated conductance gradients, while magnetospheric-origin FACs are primarily influenced by vorticities. Hence, we analyze the variation of magnetospheric-origin and ionospheric-origin FACs with MLAT. Our findings reveal that magnetospheric-origin FACs generally exhibit the structure of R1/R2 FACs, whereas ionospheric-origin FACs in the dawn and dusk sectors display high values at MLATs of 65°-69° and 67°-70°. These regions of high values are linked to intense electron precipitation and enhanced conductances. This indicates that the high values of ionospheric-origin FACs observed may be attributed to the substantial particle precipitation occurring in the auroral oval. This precipitation in the auroral oval contributes to heightened height-integrated conductances and gradients, thereby amplifying the influence of ionospheric-origin FACs. Furthermore, ionospheric-origin FACs reach a comparable level to magnetospheric-origin FACs in the high-value region, but they are significantly smaller and almost negligible in other regions. This highlights the importance of height-integrated conductance gradients and vorticities in the auroral oval, while vorticities dominate in other regions. Moreover, the intensity of auroral activity is closely associated with particle precipitation, implying a potential connection between ionospheric-origin FACs and auroral activity.

OU ET AL. 12 of 15

21699402, 2024, 6, Downloaded from https://agupubs.onlinelibrary.

Institute, Wiley Online Library on [02/04/2025]. See the Terms

5. Conclusions

We develop a complete method for calculating FACs by combining height-integrated conductances, vorticities, velocities, and geomagnetic fields. Unlike previous studies, our method addresses the limitations of assuming uniform conductances by incorporating the calculation results of height-integrated conductances. Furthermore, our approach allows for FAC calculations at a lower altitude (250 km) and provides high-resolution measurements within observable areas. Another advantage of this method lies in its ability to directly calculate and analyze the impact of ionospheric vorticity and conductance on FACs. It is important to note that our method relies on joint observations from the SuperDARN radar and DMSP/SSUSI sensor, resulting in a smaller data set than other FAC data.

Additionally, we perform statistical analysis on various parameters, including height-integrated conductances, average FACs, magnetospheric-origin FACs, and ionospheric-origin FACs. Our analysis leads to the following conclusions: (a) The distribution of average FACs exhibits a distinct large-scale structure known as R1/R2 FACs; (b) Within the auroral oval, ionospheric-origin FACs reach a comparable level to magnetospheric-origin FACs, although they are significantly smaller and almost negligible in other regions. This implies that in the auroral oval, both height-integrated conductance gradients and vorticities play equally important roles, while in other regions, vorticities dominate. Future work will involve investigating the relationship between aurora and ionospheric-origin FACs, as well as comparing our findings with alternative methods of calculating FACs.

Data Availability Statement

The raw files of SuperDARN data can be accessed via the SuperDARN data mirrors hosted by the British Antarctic Survey (https://www.bas.ac.uk/project/superdarn/#data) and the University of Saskatchewan (https://superdarn.ca). The raw SuperDARN data can be freely accessed from the British Antarctic Survey SuperDARN data mirror (https://www.bas.ac.uk/project/superdarn). The EDR-AUR data of DMSP/SSUSI were obtained from http://ssusi.jhuapl.edu. The code for the GLOW model can be found at the website http://download.hao.ucar.edu/pub/stans/glow/. The IGRF model is available at https://www.ngdc.noaa.gov/IAGA/vmod/igrf.html.

Acknowledgments

We express our gratitude to the Chinese National Arctic and Antarctic Data Center for providing us with the Radar Software Toolkit and SuperDARN data. This research was funded by the National Key Research and Development Plan of China (2022YFF0503702), the National Natural Science Foundation of China (Grants 42030203, 42374208), the Jiangsu Funding Program for Excellent Postdoctoral Talent (2023ZB459), and the Wuxi University Research Start-up Fund for Introduced Talents. We would also like to extend our appreciation to the reviewers and editors for their valuable assistance in evaluating the paper.

References

- Amm, O., Aksnes, A., Stadsnes, J., Østgaard, N., Vondrak, R. R., Germany, G. A., et al. (2005). Mesoscale ionospheric electrodynamics of omega bands determined from ground-based electromagnetic and satellite optical observations. *Annales Geophysicae*, 23(2), 325–342. https://doi.org/10.5194/angeo-23-325-2005
- Anderson, B. J., Takahashi, K., & Toth, B. A. (2000). Sensing Global Birkeland currents with Iridium engineering magnetometer data. Geophysical Research Letters, 27(24), 4045–4048. https://doi.org/10.1029/2000GL000094
- Bailey, S. M., Barth, C. A., & Solomon, S. C. (2002). A model of nitric oxide in the lower thermosphere. *Journal of Geophysical Research*, 107(A8), 1205. https://doi.org/10.1029/2001JA000258
- Bilitza, D., & Rawer, A. K. (1992). International reference ionosphere 1990. Planetary and Space Science, 40(4), 544. https://doi.org/10.1016/0032-0633(92)90174-M
- Boström, R. (1974). Ionosphere-magnetosphere coupling. Magnetospheric Physics, 45–59. https://doi.org/10.1007/978-94-010-2214-9_4
- Carter, J. A., Milan, S. E., Coxon, J. C., Walach, M.-T., & Anderson, B. J. (2016). Average field-aligned current configuration parameterized by solar wind conditions. *Journal of Geophysical Research: Space Physics*, 121(2), 1294–1307. https://doi.org/10.1002/2015JA021567
- Carter, J. A., Milan, S. E., Forsyth, C., Lester, M. E., Walach, M.-T., Gjerloev, J., et al. (2023). Mean energy flux, associated derived height-integrated conductances, and field-aligned current magnitudes evolve differently during a substorm. *Journal of Geophysical Research: Space Physics*, 128(2), e2022JA030942. https://doi.org/10.1029/2022JA030942
- Carter, J. A., Milan, S. E., Paxton, L. J., Anderson, B. J., & Gjerloev, J. (2020). Height-integrated ionospheric conductances parameterized by interplanetary magnetic field and substorm phase. *Journal of Geophysical Research: Space Physics*, 125(10), e2020JA028121. https://doi.org/ 10.1029/2020JA028121
- Chisham, G., Freeman, M. P., Abel, G. A., Bristow, W. A., Marchaudon, A., Ruohoniemi, J. M., & Sofko, G. J. (2009). Spatial distribution of average vorticity in the high-latitude ionosphere and its variation with interplanetary magnetic field direction and season. *Journal of Geophysical Research*, 114(A9), A09301. https://doi.org/10.1029/2009ja014263
- Chisham, G., & Pinnock, M. (2002). Assessing the contamination of SuperDARN global convection maps by non-F-region backscatter. Annales Geophysicae, 20(1), 13–28. https://doi.org/10.5194/angeo-20-13-2002
- Chisham, G., Yeoman, T. K., & Sofko, G. J. (2008). Mapping ionospheric backscatter measured by the SuperDARN HF radars—Part 1: A new empirical virtual height model. *Annales Geophysicae*, 26(4), 823–841. https://doi.org/10.5194/angeo-26-823-2008
- Coxon, J. C., Milan, S. E., Clausen, L. B. N., Anderson, B. J., & Korth, H. (2014a). The magnitudes of the regions 1 and 2 Birkeland currents observed by AMPERE and their role in solar wind-magnetosphere-ionosphere coupling. *Journal of Geophysical Research: Space Physics*, 119(12), 9804–9815. https://doi.org/10.1002/2014JA020138
- Coxon, J. C., Milan, S. E., Clausen, L. B. N., Anderson, B. J., & Korth, H. (2014b). A superposed epoch analysis of the regions 1 and 2 Birkeland currents observed by AMPERE during substorms. *Journal of Geophysical Research: Space Physics*, 119(12), 9834–9846. https://doi.org/10.1002/20141A020500
- Dunlop, M. W., Yang, Y. Y., Yang, J. Y., Lühr, H., Shen, C., Olsen, N., et al. (2015). Multi-spacecraft current estimates at Swarm. Journal of Geophysical Research: Space Physics, 120(10), 8307–8316. https://doi.org/10.1002/2015JA021707

OU ET AL. 13 of 15



Journal of Geophysical Research: Space Physics

- 10.1029/2024JA032708
- Escoubet, C. P., Fehringer, M., & Goldstein, M. (2001). Introduction: The cluster mission. Annales Geophysicae, 19(10/12), 1197–1200. https://doi.org/10.5194/angeo-19-1197-2001
- Freeman, M. P., Southwood, D. J., Lester, M., & Waldock, J. A. (1990). Measurement of field-aligned currents by the SABRE coherent scatter radar. In *Physics of magnetic flux ropes, geophysical monograph series* (Vol. 58, pp. 575–580). American Geophysical Union. https://doi.org/10.1029/sm058p0575
- Gjerloev, J. W., Ohtani, S., Iijima, T., Anderson, B., Slavin, J., & Le, G. (2011). Characteristics of the terrestrial field-aligned current system. Annales Geophysicae, 29(10), 1713–1729. https://doi.org/10.5194/angeo-29-1713-2011
- Green, D. L., Waters, C. L., Anderson, B. J., & Korth, H. (2009). Seasonal and interplanetary magnetic field dependence of the field-aligned currents for both Northern and Southern Hemispheres. *Annales Geophysicae*, 27(4), 1701–1715. https://doi.org/10.5194/angeo-27-1701-2009
- Green, D. L., Waters, C. L., Anderson, B. J., Korth, H., & Barnes, R. J. (2006). Comparison of large-scale Birkeland currents determined from iridium and SuperDARN data. Annales Geophysicae, 24(3), 941–959. https://doi.org/10.5194/angeo-24-941-2006
- Iijima, T., & Potemra, T. A. (1976a). The amplitude distribution of field-aligned currents at northern high latitudes observed by Triad. Journal of Geophysical Research, 81(13), 2165–2174. https://doi.org/10.1029/ja081i013p02165
- lijima, T., & Potemra, T. A. (1976b). Field-aligned currents in the dayside cusp observed by Triad. *Journal of Geophysical Research*, 81(34), 5971–5979. https://doi.org/10.1029/ja081i034p05971
- lijima, T., Potemra, T. A., Zanetti, L. J., & Bythrow, P. F. (1984). Large-scale Birkeland currents in the dayside polar region during strongly northward IMF: A new Birkeland current system. *Journal of Geophysical Research*, 89(A9), 7441–7452. https://doi.org/10.1029/ JA089iA09p07441
- Juusola, L., Milan, S. E., Lester, M., Grocott, A., & Imber, S. M. (2014). Interplanetary magnetic field control of the ionospheric field-aligned current and convection distributions. *Journal of Geophysical Research: Space Physics*, 119(4), 3130–3149. https://doi.org/10.1002/2013IA019455
- Korth, H., Anderson, B. J., & Waters, C. L. (2010). Statistical analysis of the dependence of large-scale Birkeland currents on solar wind parameters. Annales Geophysicae, 28(2), 515–530. https://doi.org/10.5194/angeo-28-515-2010
- Kosch, M. J., Scourfield, M. W. J., & Amm, O. (2001). The importance of conductivity gradients in ground-based field-aligned current studies. Advances in Space Research, 27(6–7), 1277–1282. https://doi.org/10.1016/s0273-1177(01)00203-4
- Liu, E. X., Hu, H. Q., Liu, R. Y., Wu, Z. S., Wu, M. J., Yang, H. G., & Zhang, B. C. (2012). Diurnal variation of HF radar echoes at Zhongshan Station and the influence of geomagnetic activity. *Chinese Journal of Geophysics*, 55(9), 3066–3076. https://doi.org/10.6038/j.issn.0001-5733. 2012.09.024
- McGranaghan, R., Knipp, D. J., Matsuo, T., Godinez, H., Redmon, R. J., Solomon, S. C., & Morley, S. K. (2015). Modes of high-latitude auroral conductance variability derived from DMSP energetic electron precipitation observations: Empirical orthogonal function analysis. *Journal of Geophysical Research: Space Physics*, 120(12), 11013–11031. https://doi.org/10.1002/2015JA021828
- McGranaghan, R., Knipp, D. J., Solomon, S. C., & Fang, X. (2015). A fast, parameterized model of upper atmospheric ionization rates, chemistry, and conductivity. *Journal of Geophysical Research: Space Physics*, 120(6), 4936–4949. https://doi.org/10.1002/2015JA021146
- McWilliams, K. A., Yeoman, T. K., Sigwarth, J. B., Frank, L. A., & Brittnacher, M. (2001). The dayside ultraviolet aurora and convection responses to a southward turning of the interplanetary magnetic field. *Annales Geophysicae*, 19(7), 707–721. https://doi.org/10.5194/angeo-19-707-2001
- Milan, S. E., Clausen, L. B. N., Coxon, J. C., Carter, J. A., Walach, M.-T., Laundal, K., et al. (2017). Overview of solar wind-magnetosphere-ionosphere-atmosphere coupling and the generation of magnetospheric currents. Space Science Reviews, 206(1–4), 547–573. https://doi.org/10.1007/s11214-017-0333-0
- Milan, S. E., Lester, M., Cowley, S. W. H., & Brittnacher, M. (2000). Dayside convection and auroral morphology during an interval of northward interplanetary magnetic field. *Annales Geophysicae*, 18(4), 436–444. https://doi.org/10.1007/s00585-000-0436-9
- Papitashvili, V. O., Christiansen, F., & Neubert, T. (2002). A new model of field-aligned currents derived from high-precision satellite magnetic field data. Geophysical Research Letters. 29(14), 1683, https://doi.org/10.1029/2001GL014207
- Paxton, L. J., & Anderson, D. E. (1992). Far ultraviolet remote sensing of Venus and Mars. Geophysical Monograph, 66, 113–189. https://doi.org/10.1029/GM066p0113
- Paxton, L. J., Morrison, D., Zhang, Y., Kil, H., Wolven, B. C., Ogorzalek, B. S., et al. (2002). Validation of remote sensing products produced by the Special Sensor Ultraviolet Scanning Imager (SSUSI): A far UV-imaging spectrograph on DMSP F-16. Optical Spectroscopic Techniques, Remote Sensing, and Instrumentation for Atmospheric and Space Research IV, 4485, 338–348. https://doi.org/10.1117/12.454268
- Paxton, L. J., & Zhang, Y. (2016). Far ultraviolet imaging of the aurora. In Space weather fundamentals (pp. 213–244). CRC Press. https://doi.org/10.1201/9781315368474-14
- Picone, J. M., Hedin, A. E., Drob, D. P., & Aikin, A. C. (2002). NRLMSISE-00 empirical model of the atmosphere: Statistical comparisons and scientific issues. *Journal of Geophysical Research*, 107(A12), SIA15-1–SIA15-16. https://doi.org/10.1029/2002JA009430
- Ritter, P., Lühr, H., & Rauberg, J. (2013). Determining field-aligned currents with the Swarm constellation mission. *Earth Planets and Space*, 65(11), 1285–1294. https://doi.org/10.5047/eps.2013.09.006
- Robinson, R. M., & Vondrak, R. R. (1984). Measurements of E region ionization and conductivity produced by solar illumination at high latitudes. Journal of Geophysical Research, 89(A6), 3951–3956. https://doi.org/10.1029/JA089iA06p03951
- Robinson, R. M., Vondrak, R. R., Miller, K., Dabbs, T., & Hardy, D. (1987). On calculating ionospheric conductances from the flux and energy of precipitating electrons. *Journal of Geophysical Research*, 92(A3), 2565–2569. https://doi.org/10.1029/JA092iA03p02565
- Robinson, R. M., Zhang, Y., Anderson, B. J., Zanetti, L. J., Korth, H., & Fitzmaurice, A. (2018). Statistical relations between field-aligned currents and precipitating electron energy flux. Geophysical Research Letters, 45(17), 8738–8745. https://doi.org/10.1029/2018GL078718
- Roble, R. G., Ridley, E. C., Richmond, A. D., & Dickinson, R. E. (1988). A coupled thermosphere/ionosphere general circulation model. Geophysical Research Letters, 15(12), 1325–1328. https://doi.org/10.1029/GL015i012p01325
- Slavin, J. A., Le, G., Strangeway, R. J., Wang, Y., Boardsen, S. A., Moldwin, M. B., & Spence, H. E. (2008). Space technology 5 multipoint measurements of near-Earth magnetic fields: Initial results. *Geophysical Research Letters*, 35(2), L02107. https://doi.org/10.1029/ 2007GL031728
- Sofko, G. J., Greenwald, R., & Bristow, W. (1995). Direct determination of large-scale magnetospheric field-aligned currents with SuperDARN. Geophysical Research Letters, 22(15), 2041–2044. https://doi.org/10.1029/95g101317
- Solomon, S. C. (2017). Global modeling of thermospheric airglow in the far ultraviolet. Journal of Geophysical Research: Space Physics, 122(7), 7834–7848. https://doi.org/10.1002/2017JA024314
- Solomon, S. C., & Abreu, V. J. (1989). The 630 nm dayglow. *Journal of Geophysical Research*, 94(A6), 6817–6824. https://doi.org/10.1029/ JA094iA06p06817

OU ET AL. 14 of 15

- Solomon, S. C., Hays, P. B., & Abreu, V. J. (1988). The auroral 6300 Å emission: Observations and modeling. *Journal of Geophysical Research*, 93(A9), 9867–9882. https://doi.org/10.1029/JA093iA09p09867
- Strobel, D. F., Opal, C. B., & Meier, R. R. (1980). Photoionization rates in the night-time E- and F-region ionosphere. *Planetary and Space Science*, 28(11), 1027–1033. https://doi.org/10.1016/0032-0633(80)90050-1
- Thébault, E., Finlay, C. C., Beggan, C. D., Alken, P., Aubert, J., Barrois, O., et al. (2015). International geomagnetic reference field: The 12th generation. Earth Planets and Space, 67(1), 70. https://doi.org/10.1186/s40623-015-0228-9
- Villain, J. P., Hanuise, C., & Caudal, G. (1985). A SAFARI-EISCAT comparison between the velocity of F region small-scale irregularities and the ion drift. *Journal of Geophysical Research*, 90(A9), 8433–8443. https://doi.org/10.1029/ja090ia09p08433
- Wang, H., & Lühr, H. (2021). Effects of solar illumination and substorms on auroral electrojets based on CHAMP observations. *Journal of Geophysical Research: Space Physics*, 126(2), 2169–9380. https://doi.org/10.1029/2020ja028905
- Wang, H., Lühr, H., & Ma, S. Y. (2005). Solar zenith angle and merging electric field control of field-aligned currents: A statistical study of the Southern Hemisphere. *Journal of Geophysical Research*, 110(A3), A03306. https://doi.org/10.1029/2004JA010530
- Wang, H., Yu, L., & Zheng, Z. C. (2020). Statistical study of abnormal polarity and density of field-aligned currents events. Chinese Journal of Geophysics, 63(4), 1294–1307. https://doi.org/10.6038/cjg2020N0217
- Weimer, D. R. (2001). Maps of ionospheric field-aligned currents as a function of the interplanetary magnetic field derived from dynamics explorer 2 data. *Journal of Geophysical Research*, 106(A7), 12889–12902. https://doi.org/10.1029/2000JA000295
- Xiong, C., Stolle, C., Alken, P., & Rauberg, J. (2020). Relationship between large-scale ionospheric field-aligned currents and electron/ion precipitations: DMSP observations. Earth Planets and Space, 72(147), 147. https://doi.org/10.1186/s40623-020-01286-z
- Zmuda, A. J., & Armstrong, J. C. (1974). The diurnal flow pattern of field-aligned currents. *Journal of Geophysical Research*, 79(31), 4611–4619. https://doi.org/10.1029/ja079i031p04611

QU ET AL. 15 of 15